Phasing a segmented telescope

Irina Paykin,[1] Lee Yacobi,[1] Joan Adler,[2,*] and Erez N. Ribak[1]

[1]*Department of Physics, Technion—Israel Institute of Technology, Technion City, Haifa 32000, Israel*

[2]*Computational Physics Group, Department of Physics, Technion—Israel Institute of Technology, Technion City, Haifa 32000, Israel*

A crucial part of segmented or multiple-aperture systems is control of the optical path difference between the segments or subapertures. In order to achieve optimal performance we have to phase subapertures to within a fraction of the wavelength, and this requires high accuracy of positioning for each subaperture. We present simulations and hardware realization of a simulated annealing algorithm in an active optical system with sparse segments. In order to align the optical system we applied the optimization algorithm to the image itself. The main advantage of this method over traditional correction methods is that wave-front-sensing hardware and software are no longer required, making the optical and mechanical system much simpler. The results of simulations and laboratory experiments demonstrate the ability of this optimization algorithm to correct both piston and tip-tilt errors.

I. INTRODUCTION

The angular resolution of ground-based telescopes is limited by their weight and size. Large mirrors are difficult to fabricate and mount, and the mirrors can deform due to gravity. These limitations are much more serious for space telescopes, which are restricted by launch vehicle and in-orbit constraints. Segmented and multiaperture systems allow us to go beyond this limit and have the advantage of low cost as well as light weight. If we apply the multiple-aperture approach to optical wavelengths we have to phase subapertures to within a fraction of the wavelength in order to achieve optimal performance, and this requires high accuracy of positioning for alignment of each subaperture.

The angular resolution of a telescope is given by the Rayleigh criterion

$$\Delta\theta = 1.22\frac{\lambda}{D}, \tag{1}$$

where D is the aperture diameter and λ is wavelength. Therefore, the resolution can be improved by either decreasing the wavelength or increasing the diameter of the aperture. The wavelength of observation is typically fixed; therefore, the diameter of the aperture is the only independent variable. However, large primary mirrors are difficult to fabricate and mount and for space telescopes there is a practical limit to the size of a mirror that can be stowed in current launch vehicles, for example, limited by the size of the Hubble Space Telescope. Large telescopes, such as the Keck Observatory and the future Thirty Meter Telescope, the European Extremely Large Telescope, and the James Webb Space Telescope employ arrays of hexagonal segments to create a primary mirror. The planned 25.4-m Giant Magellan Telescope is an extremely large ground-based sparse aperture telescope, which consists of seven noncontiguous circular 8.4-m primary mirror segments and an identically segmented secondary mirror [1]. The phasing system includes both edge sensors and wave-front sensors, such as capacitive edge sensors, pyramid wave-front

sensors, and a phasing camera [2], which employs the concept of the dispersed Hartmann design.

In order to phase these contiguous arrays of panels, it is possible to use mechanical means or optical means to align their edges into a continuous array [3,4], thus easing the problem of array phasing. However, this solution relies heavily on the assumption that the edges of the segments are in line with the rest of the optical surface, which requires very accurate polishing of the segment boundaries. In the case of sparse noncontiguous panels it is simply not possible to tie together panel borders. Standard wave-front sensors, such as Hartmann-Shack and curvature sensors [5–7], measure a second or third derivative of the wave front that needs to be integrated, but with separated panels this integration is not possible.

The present study concentrates on an approach for aligning multiple-aperture optical systems that is able to use only information available in the image itself. It is iterative, using a feedback loop to correct the phase errors. The idea behind this method is that we can consider the problem of multiple-aperture phasing as an optimization problem, by defining a performance metric (sharpness function) as a function of the control parameters. Optimization algorithms can be applied to find the extremum (maximum or minimum) of this sharpness function, which means that wave-front sensing hardware and software are no longer necessary, simplifying the optical and mechanical system. In order to align a multiple-aperture optical system we applied a simulated annealing (SA) algorithm [8], which is an optimization algorithm designed to find the global minimum.

Following a review of previous optimization approaches to adaptive optics systems in the next section, we present our selection of performance metric (sharpness function) in Sec. III. An introduction to salient aspects of our preferred optimization algorithm of simulated annealing is given in Sec. IV and details of the optical systems known as Golay nonredundant arrays are presented, together with a comparison of different cases, in Sec. V. Simulation results for different cost functions are given in Sec. VI, where restoration techniques are also introduced and compared. The experimental system is introduced in Sec. VII and results for three different

---

*phr76ja@tx.technion.ac.il; http://phycomp.technion.ac.il

light sources are given in Sec. VIII. The experimental system provides important proof of concept. Section IX summarizes the work.

II. PREVIOUS OPTIMIZATION APPROACHES FOR ADAPTIVE OPTICS SYSTEMS

Previous theoretical work and simulations [9] have shown that the optical problem can be mapped onto a model for crystal roughening that has provided a guide to implementation of SA. The analogy was made between columns of atoms in solid with a surface (known as a solid-on-solid model [10]) and segmented mirrors of different height and will be presented in detail in Sec. IV. The main difference is that a Hamiltonian is to be minimized, while the telescope cost function is to be maximized. Other stochastic algorithms, such as the stochastic parallel gradient descent (SPGD) [11,12] and the genetic algorithm (GA) [13], have been successfully used as the control algorithms for adaptive optics systems. For example, the GA has been applied by Yang *et al.* [14] and SPGD by Vorontsov *et al.* [15]. These algorithms have some stochastic nature, which can help the algorithm escape from local extrema. Therefore, any of the above algorithms may be a possible algorithm for control of sparse aperture active optical systems. Still, most prior applications were for continuous wave fronts, whereas here we deal with sparse ones. These optimization algorithms also have been successfully used as the control algorithms for coherent beam combining of fiber arrays [16–19]. The convergence rate of the SA algorithm was compared to other optimization algorithms by a number of authors [20,21] and these papers show that the GA is the slowest algorithm, while SA and SPGD have comparable convergence rates.

III. IMAGE SHARPENING

A crucial part of the segmented or multiple-aperture system's design is control of the optical path difference (OPD) between the segments or subapertures. Unfortunately, there is no direct method of measuring the phase of propagating light and the best we can do is to measure intensity. One way of extracting phase information from intensity measurements is interferometry, which requires the light beam to have high spatial coherence as well as a reference beam. The Hartmann-Shack and curvature sensors are preferable to interferometry because these devices do not require coherent light and a reference beam. Another random and iterative method is phase diversity [22,23] that uses images captured by an optical system, taken at zero and small defocusing, to recover optical phase information. Another form of diversity is the piston [24]. This technique has been used successfully for wave-front sensing in multiple-aperture telescopes [25]. The main disadvantages of the method are the extensive computations to obtain convergence and preference to a narrow spectral band, which leads to 2π ambiguity. The main advantage of our approach over phase diversity is that it does not suffer from this ambiguity.

In our approach to alignment of the noncontiguous or sparse aperture active optics, we consider the problem of multiple-aperture phasing as an optimization problem, by

defining a performance metric (sharpness function) as a function of the control parameters. This approach is based on the work of Muller and Buffington [26], who defined several sharpness functions that reach their maximum value only in the absence of aberrations. The sharpness function plays an important role in the optimization process and different sharpness functions can produce different results, i.e., convergence rates. It is possible to construct a sharpness metric that will take into account the properties of a specific image. In this case the optimization algorithm will be sensitive to certain image features that can improve the convergence rate of the algorithm [27]. It is also possible to create other cost functions by adding suitable constraints or penalty terms. The number of measurements required during this optimization process depends upon the optimization algorithm, sharpness function, and number of control parameters used.

We applied the following metrics assuming an object that is a point source. The irradiance at a fixed point in the image plane is given by Eq. (2) and the mean radius (MR) in Eq. (3), where r is the radial coordinate in the image plane and (u,v) are the image plane coordinates:

$$E_1 = I(u_0, v_0), \tag{2}$$

$$E_2 = E_{MR} = \frac{\int |r - \overline{r}| I(r) dr}{\int I(r) dr}, \quad \overline{r} = \frac{\int r \, I(r) dr}{\int I(r)}. \tag{3}$$

On extended objects we apply a sharpness function E_3 defined as

$$E_3 = \int du \, dv [I(u,v) - I_0]^2, \tag{4}$$

where I_0 is the average irradiance and (u,v) are image plane coordinates. Sharpness functions E_1 and E_3 increase as the quality of the image is improved and reach their maximum only in the absence of aberrations, while E_2 decreases as the quality of the image is improved and the minimum of E_2 corresponds to the smallest energy spread. Sharpness functions E_1 and E_3 can be changed by adding the minus sign and in this case the metrics will reach their minimum in the optimum mirror configuration.

IV. SIMULATED ANNEALING

Simulated annealing is an optimization algorithm designed to find the global minimum of a specific cost function, which is analogous to the Hamiltonian (energy) of the system, and is based on the physical annealing process. Annealing is a physical process whereby a solid is heated to a temperature close to its melting point and then is allowed to cool slowly. The aim is to remove internal stresses and nonuniformities and form long-range correlations and as result to achieve a structure that is as close as possible to the ground-state equilibrium configuration. The SA algorithm is a stochastic algorithm that generates random states. At each step, the values of two states (the current state and newly selected state) are compared. Cost-improving states are always accepted, while only a fraction of nonimproving states are accepted, the latter providing a mechanism of escape from local optima. The probability of accepting nonimproving states depends on the

control parameter T, which is equivalent to the temperature of the physical system. Therefore, the key algorithmic feature of SA is its ability to avoid being trapped in local minima or maxima by accepting not only the states that decrease the energy, but occasionally also some states that increase the energy to help the algorithm climb out of a local minimum. Application of this algorithm to general optimization problems was first suggested and outlined by Kirkpatrick *et al.* [8] and was based on the Metropolis algorithm [28], which was by that time a powerful tool for studying the thermodynamic equilibrium in statistical mechanical simulations.

Our first application of SA to a mosaic telescope was described in [9], with details of the mapping presented in [10]. Specifically, the analogy between the multivalleyed spin-glass energy landscape and the landscape of a solid-on-solid model and hence a mosaic telescope was presented. As described in [9], the optimization approach of [26] for a mosaic telescope is a simulated quench, which would be appropriate only if the energy valley were parabolic. A further discussion of the multivalleyed nature of the configuration space with a figure is given in [29].

We do not necessarily expect to find a totally global minimum. In both the Lennard-Jones crystal of [29] and the earlier telescope models we aimed to find a defect-free (but perturbed boundary) or an optically "good enough" state, respectively, even if it were not precisely the perfect global minimum. Reference [29] presents an educational application of simulated annealing to a small two-dimensional group of atoms interacting via a simple Lennard-Jones potential suited to a rare gas. The system was closer to the optical applications than we realized at the time, because while an infinite or periodically bounded crystal has only one perfectly ordered state of minimum energy, our system was selected for computational ease and also to mimic applications such as droplets on surfaces. With a potential suitable for the study of, for example, an aluminium drop on a sapphire substrate [30], the vapor pressure is so low that atoms will not escape, but the Lennard-Jones system has a high vapor pressure, so many or even most atoms will disappear into the surroundings at room temperature and pressure. In order to minimize the technical complications of periodic boundary conditions, we chose to use the unphysical boundary condition of reflecting boundaries, where each atom saw ghost particles that were mirror images of the actual bulk neighbors. This led to the situation where a nice looking crystal with minor boundary perturbations was achieved and hence we were satisfied with a good enough state very close to the global energy minimum that would have perfect boundaries. We obtained similar results in the telescope case, where we may not have the absolute global minimum but rather the good enough, which is also reminiscent of actual laboratory spin-glass materials (see [31] for a discussion of the difference between laboratory and computational spin glasses).

Each step of the SA algorithm can be described as follows. Given a current state i of the system with energy E_i, a new state j is then generated by a small perturbation following some probability distribution. Then the energy difference $\triangle E = E_j - E_i$ between the previous state energy E_i and the new state energy E_j is calculated and if the energy difference is negative, then the new state is always accepted. If the energy

difference is positive, then depending on the temperature, there is a chance that the state will be accepted with probability equal to $\exp(-\triangle E/T)$; otherwise the perturbation is returned to the previous state. After a sufficiently large number of iterations the system will eventually reach the equilibrium state at temperature T. Then T is lowered again. The temperature is reduced between iterations according to the exponential schedule $T_{i+1} = \gamma T_i$, where γ is the cooling rate factor, which we chose to be 0.99. In this homogeneous algorithm that we have chosen, we stop at each temperature until thermalization is achieved. In contrast, in an inhomogeneous algorithm the temperature would drop at each and every step, but at a much slower rate. The total number of steps is similar for the two methods [32]. The system is able to climb out of local minima, due to the randomness of state configurations and the variations in temperature. For SA one must provide parameters such as the initial temperature and the cooling schedule, which can have a significant impact on the algorithm's convergence and speed. In the present study the probability distributions were uniform [0,1] random numbers and we cooled very slowly. Further technical details can be found in [32,33].

V. OPTICAL MODEL

We carried out and analyzed computer simulations in order to gain a better understanding of the physical system and to examine the ability of the SA algorithm to align multiple-aperture systems. With Fourier optics [34] we can describe the imaging process as a series of Fourier transforms. A two-dimensional Fourier transform on the complex pupil function simulates the effect of Fraunhofer diffraction and can provide the point spread function (PSF) of the system. In our simulation model the telescope pupil is considered as consisting of N identical circular and nonoverlapping subapertures with unit reflectivity. The complex pupil function $W(x,y,\lambda)$ is given by a sum over the subaperture functions

$$W(x,y,\lambda) = \sum_{n=1}^{N} C(x - x_n, y - y_n) \exp[i\phi_n(x,y,\lambda)], \quad (5)$$

where (x,y) are the pupil plane coordinates, C is the shape of subaperture, $\phi_n(x,y,\lambda)$ is the contribution of the phase of each subaperture n that depends on the wavelength λ, and (x_n,y_n) is the center coordinate of the nth subaperture.

We only considered piston and tip-tilt aberrations, assuming rigid subapertures. Each array element carries a piston error P_n represented by

$$P_n = \exp\left(\frac{2\pi i}{\lambda} 2p_n\right) = \exp(2ikp_n), \quad (6)$$

where p_n is the height of the nth subaperture, measured from the same reference plane, and $k = 2\pi/\lambda$ is the wave number. If a subaperture moves from its ideal position, by a distance Δp, the light travels this additional distance twice, so the OPD is $2p$. The tip-tilt error is a result of rotations in the x and y axes of each subaperture about its center. The tip-tilt error of the nth subaperture is given by

$$\text{TT}_n = \exp\{ik[\alpha_n(x - x_n) + \beta_n(y - y_n)]\}, \quad (7)$$

where α_n and β_n are the subaperture gradients in the x and y directions, respectively. Therefore, if we take into account only piston and tip-tilt errors, the pupil function can be written as

$$W(x,y,\lambda) \sum_{n=1}^{N} C(x - x_n, y - y_n)\exp(2ikp_n)$$

$$\times \exp\{ik[\alpha_n(x - x_n) + \beta_n(y - y_n)]\}. \quad (8)$$

For a simple flat spectral density, the intensity distribution on the detector from a point source or PSF is

$$\text{PSF}(u,v) = \int_{\lambda_1}^{\lambda_2} |U(u,v,\lambda)|^2 d\lambda, \quad (9)$$

where (u,v) are angular image plane coordinates and U is the electromagnetic field at each wavelength that can be written as the Fourier transform of the pupil function

$$U(u,v,\lambda) = \mathcal{F}\{W(x,y,\lambda)\}. \quad (10)$$

If we define $U_n(u,v,\lambda)$ as the field of the nth segment, then the Fourier transform gives [Eqs. (8) and (10)]

$$U_n(u,v,\lambda) = A(u - \alpha_n, v - \beta_n)\exp[ik(2p_n + x_n u + y_n v)]. \quad (11)$$

For circular subapertures the amplitude is

$$A(u,v,\lambda) = D\frac{J_1(\pi D\sqrt{u^2 + v^2}/\lambda)}{2\sqrt{u^2 + v^2}} \quad (12)$$

and the combined intensity

$$I(u,v,\lambda) = |U(u,v,\lambda)|^2 = \sum_{l=1}^{N}\sum_{m=1}^{N} U_l(u,v,\lambda)U_m^*(u,v,\lambda)$$

is

$$I(u,v,\lambda) = \sum_{l=1}^{N}\sum_{m=1}^{N} A_{lm}(u,v,\lambda)$$

$$\times \exp[ik(\Delta x_{lm}u + \Delta y_{lm}v + 2\Delta p_{lm})], \quad (13)$$

where $(\Delta x_{lm}, \Delta y_{lm})$ are the vector separations between pairs of subaperture centers, $\Delta p_{lm} = p_l - p_m$, and

$$A_{lm}(u,v,\lambda) = A(u - \alpha_l, v - \beta_l, \lambda)A(u - \alpha_m, v - \beta_m, \lambda). \quad (14)$$

Finally we have

$$I(u,v,\lambda) = \sum_{l=1}^{N}\sum_{m=l+1}^{N} 2A_{lm}(u,v,\lambda)$$

$$\times \cos[k(\Delta x_{lm}u + \Delta y_{lm}v + 2p_{lm})] + \sum_{l=1}^{N} A_{ll}. \quad (15)$$

The combined intensity $I(u,v,\lambda)$ of any multiaperture array consisting of N identical phased subapertures is given by Eq. (16), where $(\Delta x_n, \Delta y_n)$ are the vector separations between pairs of subaperture centers. A sparse aperture system, consisting of N subapertures, has $N(N-1)/2$ baselines (subaperture pairs) and for a nonredundant array geometry each subaperture pair produces a fringe pattern at different spatial frequency.
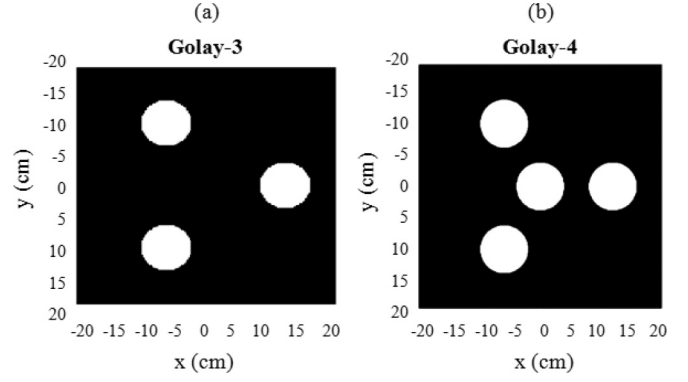

FIG. 1. System configurations: Golay-3 and Golay-4 nonredundant arrays.

Phased subapertures here mean that mirrors adjust such that the reflected wave front has zero phase difference across the whole telescope surface:

$$I(u,v,\lambda)$$

$$= [A(u,v,\lambda)]^2 \left\{ N + 2\sum_{n=1}^{N(N-1)/2} \cos[k(\Delta x_n u + \Delta y_n v)] \right\}. \quad (16)$$

In the case of incoherent illumination and an extended object, the Fourier transform of the image intensity distribution $G_I(f_x, f_y)$ is

$$G_I(f_x, f_y) = \int_{\lambda_1}^{\lambda_2} G_O(f_x, f_y, \lambda)\text{OTF}(f_x, f_y, \lambda)d\lambda, \quad (17)$$

where $G_O(f_x, f_y, \lambda)$ is the object Fourier transform, $\text{OTF}(f_x, f_y, \lambda)$ is the optical transfer function (OTF), which is the autocorrelation of the complex pupil function $W(x,y,\lambda)$, and (f_x, f_y) are the spatial frequency coordinates.

In simulations, we use two multiple-aperture configurations, the Golay-3 and Golay-4 (Fig. 1), in support of the experimental system (Sec. VIII). Golay arrays are sparse arrays with compact nonredundant autocorrelations [35]. The potential advantage of these arrays is that they allow maximizing the spatial frequency bandwidth by the widest spread of subapertures that avoids zeros in the OTF. They represent the highest possible resolution for a fixed number of subapertures. The OTF of multiple-aperture arrays has significantly reduced modulation and suffers from contrast loss in the middle range spatial frequencies as shown in Fig. 2(a), while the OTF of an ideal aberration-free filled circular aperture is a monotonically decreasing function as depicted in Fig. 2(b). Therefore, multiple-aperture systems will generally produce images with significantly reduced contrast compared to a filled aperture. In order to recover some of this lost image quality, an appropriate filtering technique can be applied. Therefore, image reconstruction is crucial in multiple-aperture imaging. In Fig. 2(a) the middle blob corresponds to all possible vectors connecting two points on the same subaperture. The side blobs correspond to all possible vectors that connect one point on one subaperture with another point on the other subaperture. It can be seen that the blobs
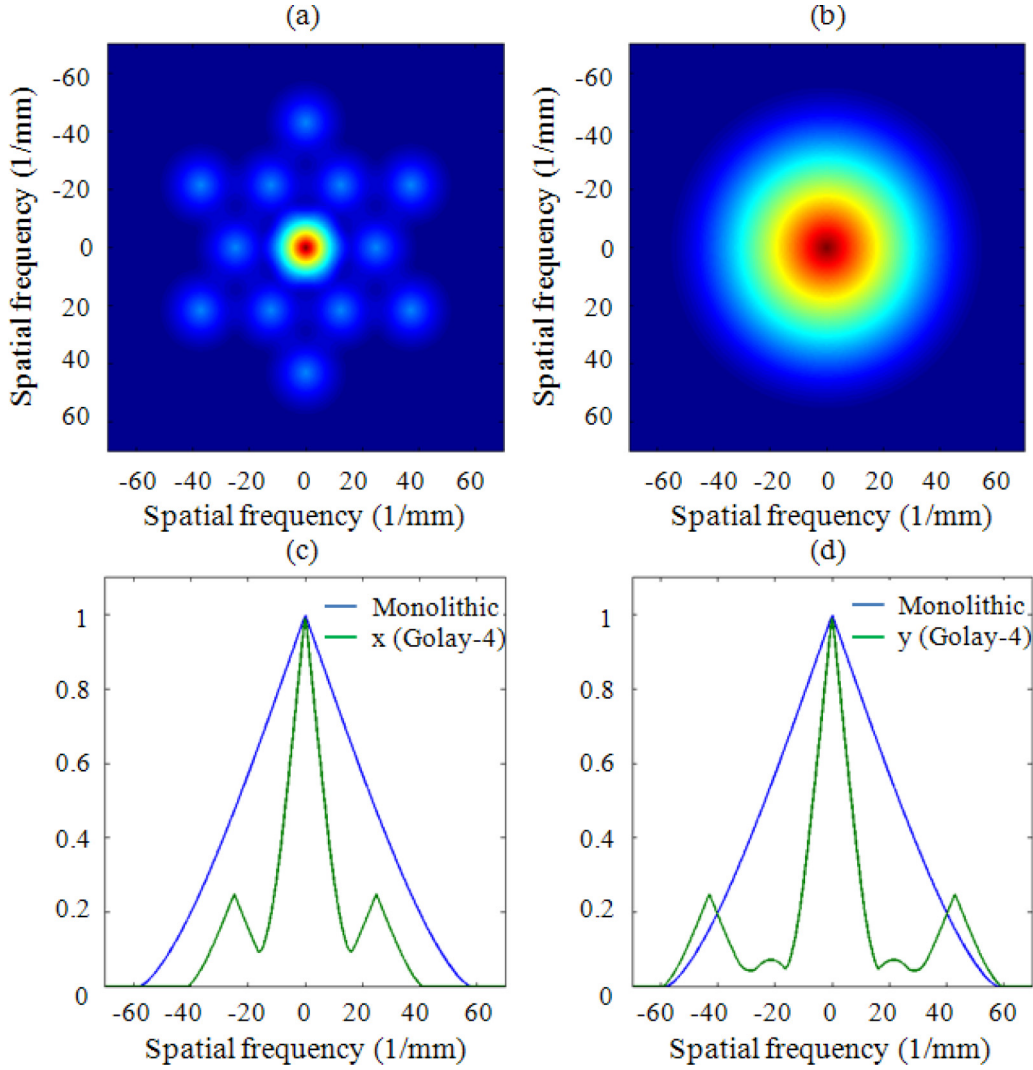
FIG. 2. (Color online) (a) and (b) The OTF of a nonredundant Golay-4 array and of an ideal aberration-free filled circular aperture of the same size. (c) and (d) Corresponding cross sections of the Golay-4 and of the filled circular aperture in the f_x and f_y directions.

are centrally bright and dropping off toward the edge. The corresponding cross sections of the Golay-4 and filled aperture in the f_x and f_y directions are shown in Figs. 2(c) and 2(d). Detailed information about how the form of the PSF and OTF varies with applied aberrations can be found in [36].

VI. RESULTS OF SIMULATIONS

The simulations were divided into two parts. In the first part SA was investigated on a point source and in the second part the performance of SA on the extended image was studied. The behavior of SA under different cost functions was examined and we saw that different image cost functions can produce different results. The image improvement was measured by the Strehl ratio (SR), which is the actual irradiance at the PSF peak divided by the maximum irradiance possible. The SR can be a good estimate of the variance of the wave-front phase across the exit pupil of the system. It is related to the wave-front error through the extended Marechal approximation [6]

$$SR \approx \exp(-\sigma^2), \tag{18}$$

where $\sigma 1$ is the root mean square wave-front error in radians.

For the point source we investigated the performance of SA on two different cost functions, the irradiance at a fixed point in the image plane [E_1, Eq. (2)] and the mean radius [E_2, Eq. (3)]. We began the simulations by initializing the mirrors' actuators with random values. After that, sequential changes to the mirror actuators were applied and the corresponding image was calculated and its quality evaluated by the cost function. This process is repeated until the image quality is considered acceptable. The optimization process was performed for each cost function over 20 different initial phase realizations; the phase was added by changing the heights of mirror actuators. The image of the point source (PSF) was modeled within a bandwidth of 500 nm, centered at 600 nm. We use ten random wavelengths to simulate this bandwidth. It is possible to remove the tilt degeneracy by looking at the irradiance at a fixed point in the image plane, but piston degeneracy cannot be removed and the mirrors can reach any flat state.

Simulation results for the irradiance at a fixed point in the image plane and comparison between different sharpness
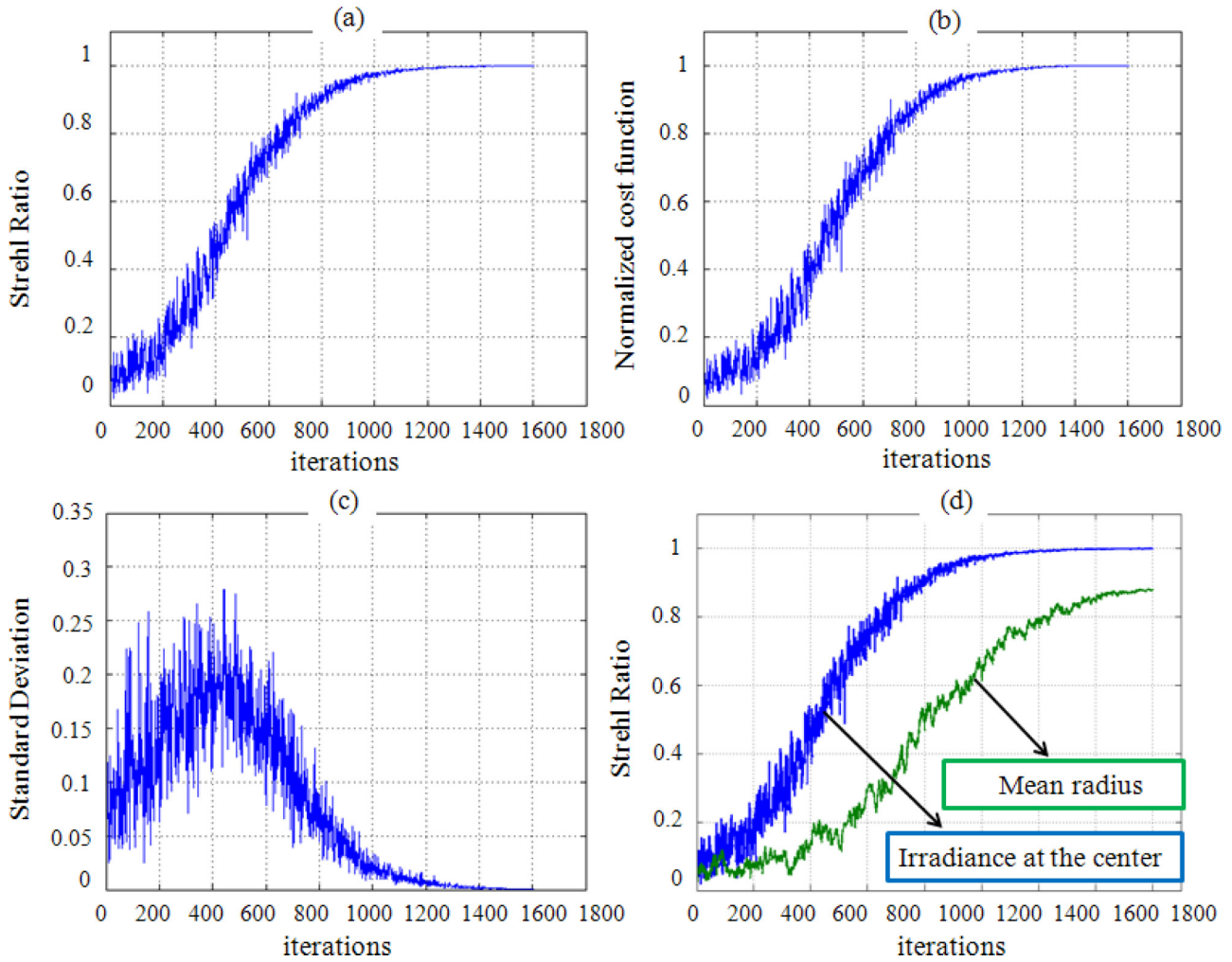
FIG. 3. (Color online) Optimization process during 1600 iterations averaged over 20 different phase realizations for the Golay-3 array and comparison between correction abilities of different image-quality metrics: (a) Strehl ratio, (b) average cost function E_1, (c) standard deviation, (d) comparison between correction abilities of image-quality metrics, the irradiance at a fixed point E_1 in the image plane (2) versus the MR (3).

functions [E_1, Eq. (2), and MR, Eq. (3)] are shown in Fig. 3. The system configuration used for these simulations is Golay-3, as illustrated in Fig. 1(a). The averaged SR for the irradiance at a fixed point in the image plane is shown in Fig. 3(a). The corresponding averaged cost function and standard deviation evolution curves are presented in Figs. 3(b) and 3(c), respectively. This averaged cost function is normalized to be 1 in the optimal case. As was explained above, the SR can be used for comparison between correction abilities of image-quality metrics. Shown in Fig. 3(d) are the corresponding averaged SR evolution curves, averaged over 20 different initial realizations of the mirrors actuators, for the irradiance at a fixed point in the image plane [E_1, Eq. (2)] and MR [Eq. (3)]. From this figure we see that different cost functions can produce different results and the irradiance at a fixed point in the image plane is a better metric for the point source than the MR.

The next phase of the simulations was to examine the performance of SA on an extended image. Figure 4 illustrates the typical behavior of SA when the energy is calculated over the whole image using cost function E_3 [Eq. (4)]. The object

used for this study is the 1951 USAF resolution test chart, which shown in Fig. 4(a). The chart consists of groups of three bars. The smallest of these bars for which the imaging system can differentiate between two bars is its resolution limit. Images were simulated for a Golay-4 configuration, as shown in Fig. 1(b) at a bandwidth 1 μm, centered at 1.5 μm. The initial image before optimization and after optimization is given in Figs. 4(b) and 4(c), respectively. In addition, the image from the aberration-free filled circular aperture of the same size is shown in Fig. 4(d). Sparse aperture systems have significantly reduced modulation relative to a filled aperture, as shown in Fig. 2, and as result will produce images with significantly reduced contrast compared to the filled aperture. Figure 4(c) illustrates that image of resolution target after optimization is of low contrast and blurred. In order to recover the image quality, an appropriate filtering technique can be applied, such as Wiener-Helstrom, Lucy-Richardson, or blind deconvolution [37]. In Fig. 5 we show a comparison between two different restoration techniques, the blind deconvolution (left) and Lucy-Richardson (right) methods.
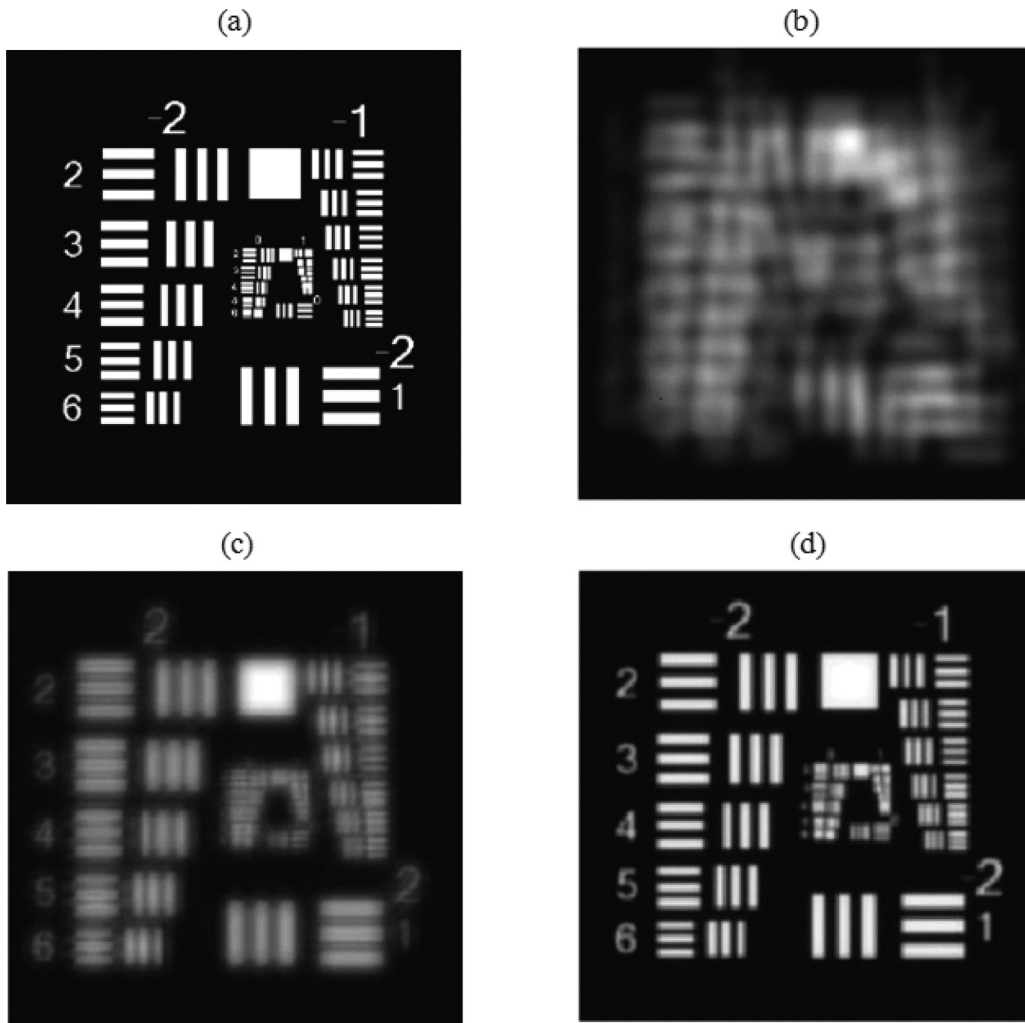
FIG. 4. Performance of SA on an extended image: (a) 1951 USAF resolution test chart, (b) initial image before optimization, (c) image after SA optimization cost function E_3 (4), and (d) image from ideal aberration-free filled circular aperture of the same size.

VII. EXPERIMENTAL SYSTEM

In parallel with the simulations, we constructed two systems in the laboratory. The initial one was composed of four separate 3-in. spherical mirrors with a focal length of 18 in. [Fig. 6(a)]. Each mirror had three piezoelectric bimorph bending actuators (Johnson Matthey 427.YYY4.50N), 120° apart, which allow it to correct piston, tip, and tilt errors, and three screws for manual
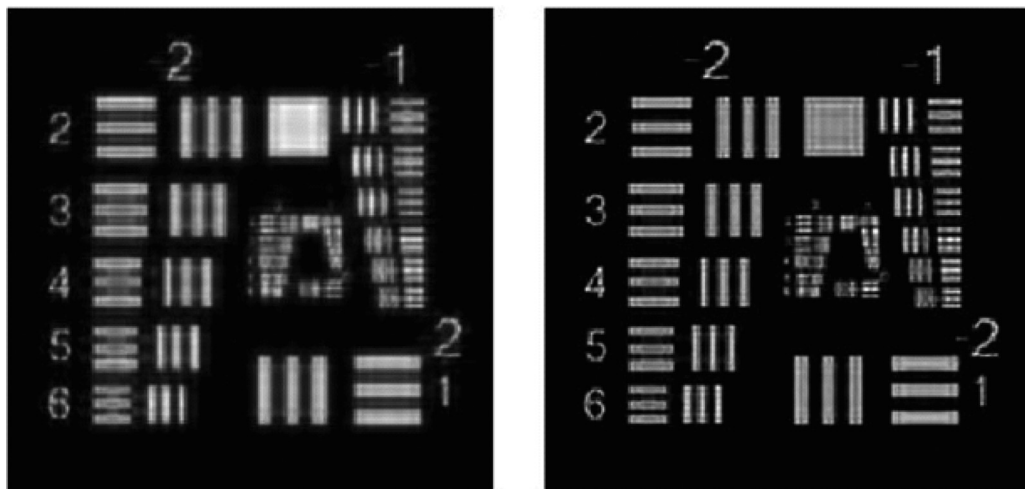

FIG. 5. Comparison between blind deconvolution (left) and the Lucy-Richardson method (right), applied to the previous result of Fig. 4(c).
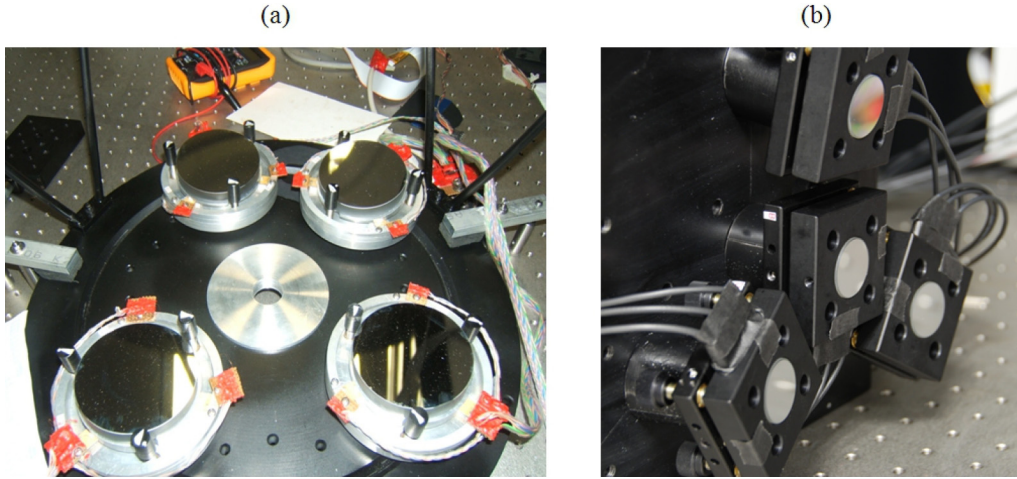
FIG. 6. (Color online) Experimental systems: (a) first system and (b) second system, the Golay-4 nonredundant array.

coarse tuning, also 120° apart. The mirrors are arranged on a large radius creating a diluted spherical mirror with a 13-in. diameter and an f-number of 1.4 with 12 actuators. This system functioned well, but suffered from vibrations and turbulence effects owing to its size, which did not allow us to work with wideband sources.

The second system is more compact, composed of four separate 1-in. spherical mirrors with a 10-in. focal length, as shown in Fig. 6(b), where each mirror is attached to three motorized piezoelectric actuators (ThorLabs KC1-PZ/M) with a translation length of several microns. The actuators are capable of subwavelength steps that allow accurate positioning of each mirror with the three degrees of freedom of a spherical surface. The four mirrors were designed in a Golay-4 nonredundant array Fig. 1(b) with a diameter of 6.5 in. and an f-number of 1.5 with 12 actuators. The system was coarse tuned until the first interference fringes from a light-emitting diode (LED) source were observed. Both systems were driven with a 16-bit D2A (MC USB-3114), which was amplified by a multichannel adaptive optics amplifier (WaveScope WFS-01-DFM) allowing translation of tens of nanometers. Both systems were also read out by a PCO pixelfly 640×480 black-and-white camera with a pixel size of 10 μm^2. Since we used spherical optics components, in both systems we put our source and camera at the center of curvature of the sphere, separated by a beam splitter. For that configuration we were not expecting optical aberration. Because of the low f-number of the system we had to use a magnifying objective in front of the camera in order to expand the interference fringes spacing beyond a pixel size.

It should be remarked that when working with a monochromatic source such as a laser, we cannot expect the system to correct piston errors since the improvement of visibility even along tens of microns suffers from 2π ambiguity and is beneath the noise of any practical system. For a similar reason, we cannot correct the piston error with a wideband source if the initial error is much larger that the source coherence length. In this case the visibility itself is governed by the noise. If we want to phase the system when starting with a large piston error we should start working with a narrow-band filter and broaden it during the calibration process. We chose to use different

sources instead. Working with a wideband source, the fringes contrast is too low to be identified by the eye and can be observed only with the assistance of a camera and computer.

We have used three light sources. In the first system we worked with a simple diode laser, where the beam was broadened by a microscope objective. In the second system we used a 617 ± 18 nm high power LED source (Thorlabs M617F1) and a tungsten-halogen thermal white source, both brought to the system with multimode fiber optics. The end of the fiber, serving as a source, does not allow proper focusing: The modes carried along the fiber change shape during focusing through and into the fiber edge.

VIII. RESULTS OF EXPERIMENT

A. Laser source

We used a diode laser in the first system. We began this experiment with manual coarse calibration, where images from two of the mirrors lie at the same place, while the third image is deflected [Fig. 7(a)]. As mentioned, we cannot expect the system to correct piston-type errors with a monochromatic source; therefore we will focus on the tip-tilt errors. Figures 7(a)–7(c) were taken during the progress of the algorithm at the points marked on the graph. In Fig. 7(b) all images already overlapped, but the PSF is smeared like a tip-tilt error effect. It seems as if the tip-tilt errors were corrected because the PSF is sharp and clear by the end of the execution (point *C*). During this experiment, the system suffered from strong vibrations. In order to overcome those vibrations we took a series of pictures at each location and averaged over the best fifth of them. This experiment ended before converging to the final state because of a mechanical problem, but despite this problem, we observe an explicit improvement of the PSF. Figures 7(d) and 7(e) are simulations of three mirrors' intensity PSF with and without tip-tilt errors.

B. The LED source

The images with the LED source are smeared as a consequence of using an extended source of a wide spectrum. Therefore, we cannot identify interference fringes by eye.
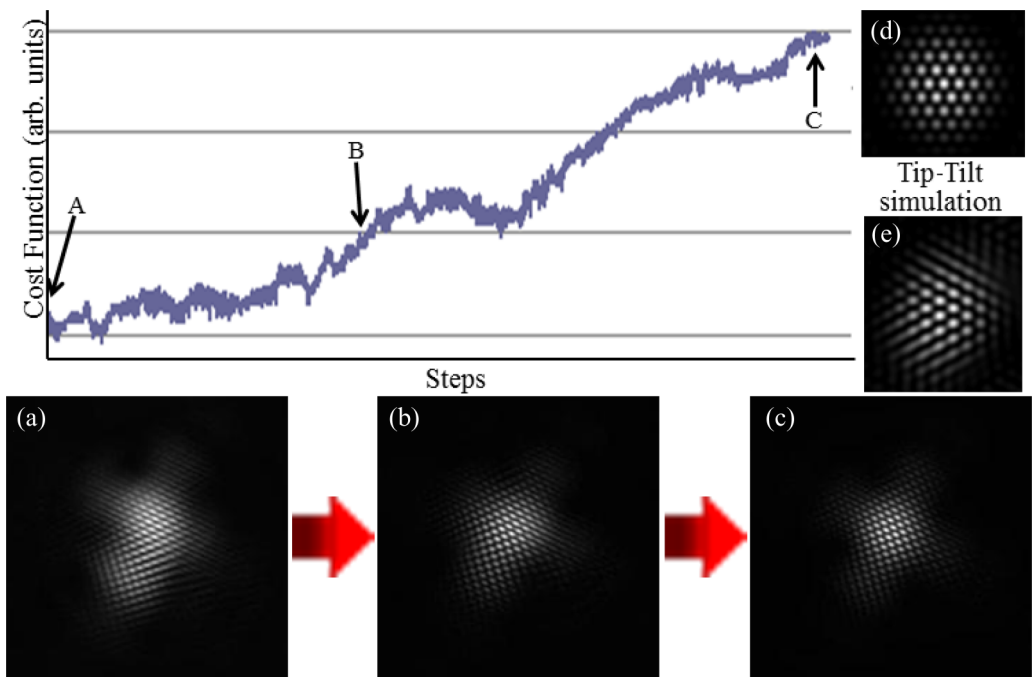
FIG. 7. (Color online) Convergence with a laser diode in the first system with three mirrors. The graph shows the cost function value during the operation of the algorithm. (a)–(c) Images of the system during the operation, at the times indicated by the arrows. (d) and (e) Numerical PSF without and with tip-tilt error, respectively.

Instead we look at the Fourier transform of the image, letting the computer identify the spatial frequencies of the fringes. Figure 8 shows details from an execution of the algorithm with a LED source. The starting point was when all spots overlapped. In the beginning the temperature was very high and almost every suggested step was accepted. This meant that the system almost made a random walk in its phase space and the cost function decreased. At point *A* the temperature reached
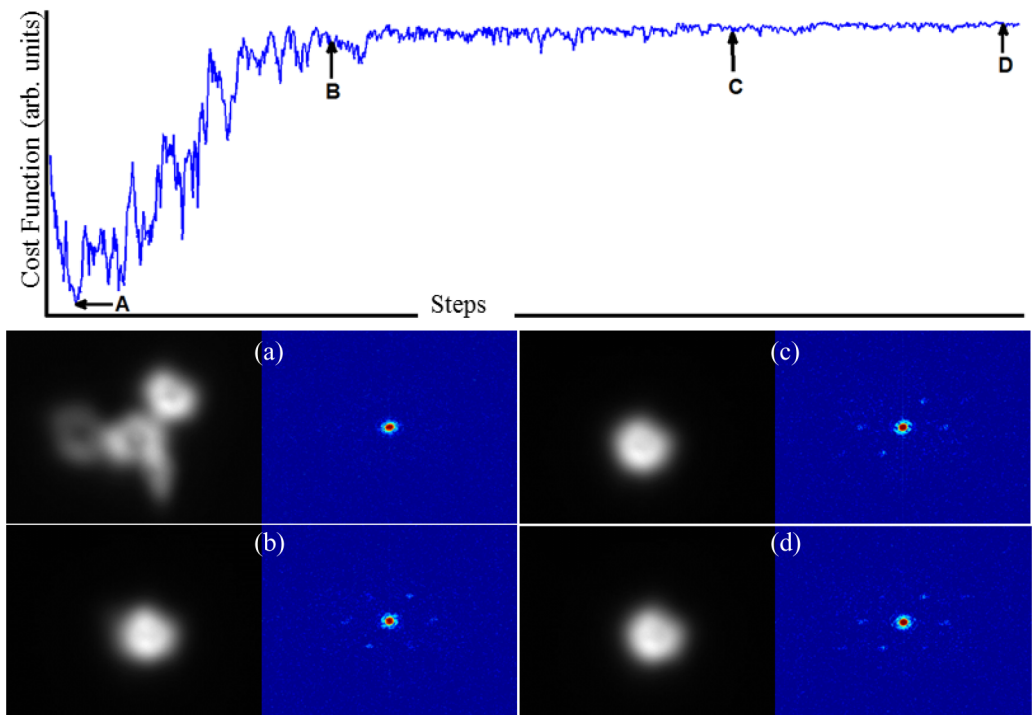

FIG. 8. (Color online) Simulated annealing convergence with a LED source, the Golay-4 configuration. The graph shows the cost function, the arrows indicating the place where the images were taken. (a)–(d) Images and their logarithmic Fourier transforms during the operation of the algorithm. As is visible in (a), one of the panels was not fully illuminated, but the system, being immune to such errors, still converged.
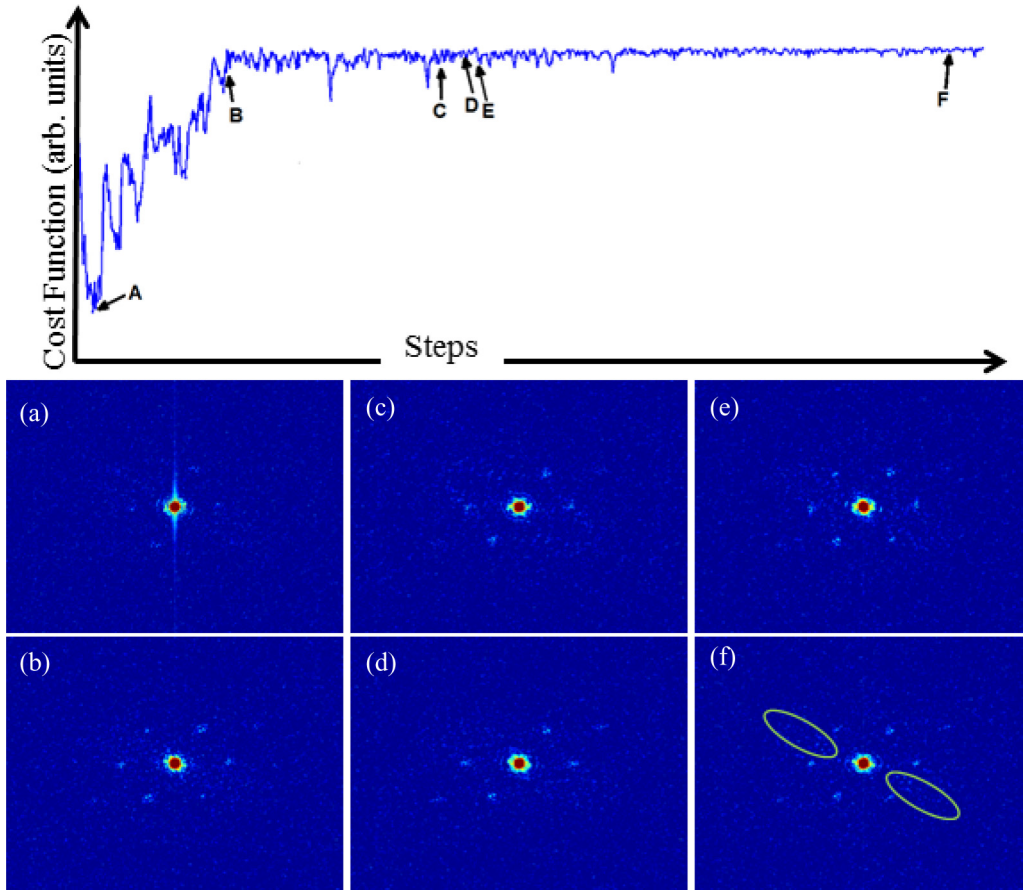
FIG. 9. (Color online) Illustration of algorithm operation with a LED source after manual connection and restart. The graph shows the cost function, with indications of the times where the images shown were taken. (a)–(f) Fourier transforms of the corresponding images. The ellipses in (f) show regions that began to be active near the end of the process.

a working value and the cost function started to improve. By point B the algorithm succeeded in stacking all images and achieving an explicit interference pattern between each of the three outer mirrors and the central one. The algorithm kept searching, relinquishing one of the interference patterns in order to find another pattern between two of the outer mirrors as appears in Fig. 8(c). By the end of the process (point D) the algorithm succeeded in finding all patterns, but with different sharpness. As we see, we cannot distinguish by eye between the images of Figs. 8(b)–8(d). In order to overcome the limited translation length of the actuators we ran the system several times in a similar way in order to attain the required coarse manual adjustment to the mirrors.

After readjusting the mirrors we executed the system again. In Fig. 9 we see that even for the lowest value of the cost function (point A), the program can still recognize low-contrast interference patterns. During the optimization process at points $B - E$ the algorithm found and lost interference patterns while improving their contrast and by the end all of them appeared with a better contrast than we could see before the readjustment, in Fig. 8. The ellipses in Fig. 9(e) are the areas in Fourier space that just start to be active during the last stage of the algorithm's operation. This might indicate that another two mirrors started to be phased, but apparently the piston error is larger than the translation length and the system cannot fix it without a prior readjustment.

To summarize, the smeared picture did not allow us to see the improvement by eye or allow us to estimate the tip-tilt errors; however, we see that the algorithm collected all images and stacked them together, performed a search for an interference pattern, and then increased the fringes contrast. The improvement of contrast indicates correction of piston errors. We should note that initially we did not succeed in phasing all mirrors; one of the outer mirrors was not phased with the two others outer mirrors, due to uneven illumination, which reduced the signal-to-noise ratio on the outer elements [Fig. 8(a)].

C. White-light source

The images taken with a white-light source suffer from the same smearing problem as the images taken with the LED source. Because of the short coherence length, the interference fringes had lower contrast and the system was much more sensitive to noise. Therefore, in addition to showing the Fourier transform of images during the system operation, we also summed over several images around each step in order to reduce the noise and reveal the interference pattern appearing in the system. Figure 10 illustrates the optimization process using the white source. Two more points can be concluded from our observations from Fig. 10. The elongation of the Fourier lobes is a direct result of using a wideband source,
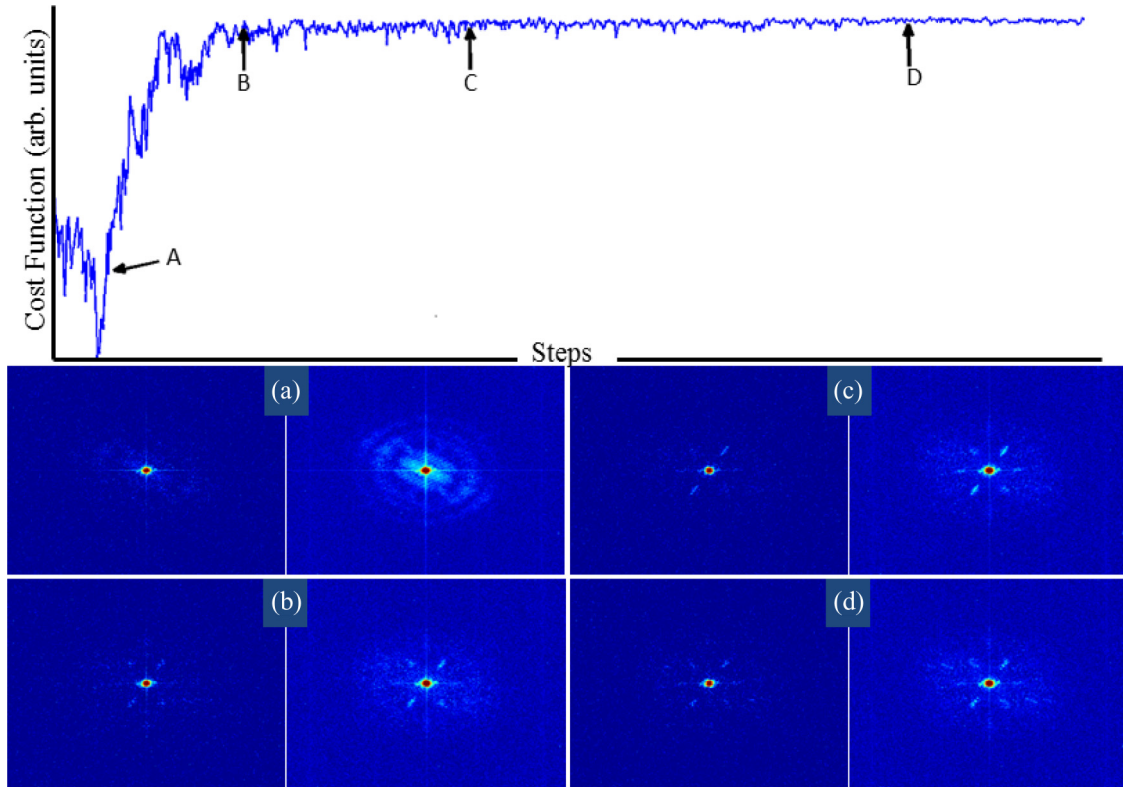
FIG. 10. (Color online) Illustration of algorithm convergence with the white source. The graph shows the cost function, the arrows indicating the places where the photographs were taken. (a)–(d) On the left is a logarithmic Fourier transform of the images during the algorithm operation. On the right is the average over several images. Note the spectral elongation (15).

where each wavelength creates an interference pattern slightly stretched compared to the others [Eq. (15)]. The second point is that the whole pattern seems to be slightly shrunk when compared to the LED source images. This is a result of changing magnification in the system. In Fig 10 we again see the process of phasing up more and more mirrors and an increase of the fringe contrast until we see the same interference patterns as with the LED source. With the white source we see again that even when starting in a state where the program could not recognize fringes, the algorithm succeeded in phasing the mirrors. The limited translation of the actuator did not allow us to estimate how well the system was phased. Yet the algorithm succeeded in improving the alignment while using only a white source.

IX. CONCLUSION

To summarize, the SA algorithm achieved good results in converging into a close to global optimum in simulations. These results prove that SA can be successfully used for alignment of segments of sparse aperture telescopes and allows us to correct degrees of freedom in our system such as tilt and piston. The behavior of SA under different cost functions was examined and we saw that different image cost functions can produce different results. Additional experiments and simulations should be performed in order to study the algorithm convergence abilities with regard to the different cost functions and the observed image properties. Also, further work is needed to compare the different optimization algorithms. The main advantage of this method is that no prior knowledge of the optical system is needed and the only necessary input is the images acquired in each step. The experimental work was focused on proving the concept and not on improving the algorithm efficiency, but this is an important conclusion by itself. With LED and white sources we see that even when starting in a state where the program could not recognize fringes, the algorithm succeeded in aligning the telescope. Most of the experimental convergence trials lasted 6000–12 000 steps and it took from 20 min to a few hours to converge. This was dependent on the exposure time of the camera, which in turn depended on the source intensity. Under turbulence, the contrast should be poorer (but not disappear, especially in the Fourier domain), which means that this method can be applied to ground-based segmented telescopes without actually measuring the locations of the segments.

[1] A. H. Bouchez, B. A. McLeod, D. S. Acton, S. Kanneganti, E. J. Kibblewhite, S. A. Shectman, and M. A. van Dam, Proc. SPIE **8447**, 84473S (2012).

[2] S. Kanneganti, B. A. McLeod, M. P. Ordway, J. B. Roll, S. A. Shectman, A. H. Bouchez, J. Codona, R. Eng, T. M. Gauron, F. Handte, T. J. Norton, P. Streechon, and D. Weaver, Proc. SPIE **8447**, 844752 (2012).

[3] G. Chanan, M. Troy, F. Dekens, S. Michaels, J. Nelson, T. Mast, and D. Kirkman, Appl. Opt. **37**, 140 (1998).

[4] G. Chanan, C. Ohara, and M. Troy, Appl. Opt. **39**, 4706 (2000).

[5] F. Roddier, Appl. Opt. **27**, 1223 (1988).

[6] J. W. Hardy, *Adaptive Optics for Astronomical Telescopes* (Oxford University Press, Oxford, 1998).

[7] A. Talmi and E. N. Ribak, J. Opt. Soc. Am. A **21**, 632 (2004).

[8] S. Kirkpatrick, C. D. Gelatt Jr., and M. P. Vecchi, Science **220**, 671 (1983).

[9] E. N. Ribak, J. Adler, and S. G. Lipson, J. Phys. A: Math. Gen. **23**, L809 (1990).

[10] J. Adler, Physica A **168**, 646 (1990).

[11] M. A. Vorontsov and G. W. Carhart, Opt. Lett. **22**, 907 (1997).

[12] M. A. Vorontsov and V. P. Sivokon, J. Opt. Soc. Am. A **15**, 2745 (1998).

[13] D. E. Goldberg, *Genetic Algorithms in Search, Optimization and Machine Learning* (Addison-Wesley, Reading, 1989).

[14] P. Yang, Y. Liu, W. Yang, M. Ao, S. Hu, B. Xu, and W. Jiang, Chin. Opt. Lett. **5**, 497 (2007).

[15] M. A. Vorontsov, G. W. Carhart, M. Cohen, and G. Cauwenberghs, J. Opt. Soc. Am. A **17**, 1440 (2000).

[16] L. Liu and M. A. Vorontsov, Proc. SPIE **5734**, 138 (2005).

[17] P. Zhou, Z. Liu, X. Wang, Y. Ma, and H. Ma, IEEE J. Sel. Top. Quantum Electron. **15**, 248 (2009).

[18] T. Weyrauch, M. A. Vorontsov, G. W. Carhart, L. A. Beresnev, A. P. Rostov, E. E. Polnau, and J. J. Liu, Opt. Lett. **36**, 4455 (2011).

[19] P. Zhang, Y. Guan, X. Xie, J. Zhou, L. Yan, and K. Sing, Opt. Express **18**, 2995 (2010).

[20] S. Zommer, E. N. Ribak, S. G. Lipson, and J. Adler, Opt. Lett. **31**, 939 (2006).

[21] H. Yang and X. Li, Opt. Laser Technol. **43**, 630 (2011).

[22] R. G. Paxman, T. J. Schulz, and J. R. Fienup, J. Opt. Soc. Am. A **9**, 1072 (1992).

[23] R. A. Gonsalves, Opt. Eng. **21**, 215829 (1982).

[24] M. R. Bolcar and J. R. Fienup, Appl. Opt. **48**, A5 (2009).

[25] F. Cassaing, B. Sorrente, L. Mugnier, G. Rousset, V. Michau, I. Mocoeur, and F. Baron, Proc. SPIE **6268**, 62683A (2006).

[26] R. Muller and A. Buffington, J. Opt. Soc. Am. **64**, 1200 (1974).

[27] J. Fienup and J. Miller, J. Opt. Soc. Am. A **20**, 609 (2003).

[28] N. Metropolis, A. Rosenbluth, M. Rosenbluth, A. Teller, and E. Teller, J. Chem. Phys. **21**, 1087 (1953).

[29] A. Silverman and J. Adler, Comput. Phys. **6**, 277 (1992).

[30] A. Hashibon, J. Adler, M. W. Finnis, and W. D. Kaplan, Comput. Mater. Sci. **24**, 443 (2002).

[31] J. Adler, A. C. D. van Enter, and A. B. Harris, Phys. Rev. B **38**, 11405 (1988).

[32] I. Paykin, M.Sc. thesis, Technion, 2014, available at http://www.graduate.technion.ac.il/Theses/Abstracts.asp?Id=27315

[33] L. Yacobi, M.Sc. thesis, Technion, 2013, available at http://www.graduate.technion.ac.il/Theses/Abstracts.asp?Id=27764

[34] J. Goodman, *Introduction to Fourier Optics*, 3rd ed. (Roberts, Greenwood Village, 2004).

[35] M. Golay, J. Opt. Soc. Am. **61**, 272 (1971).

[36] N. Miller, M. Dierking, and B. Duncan, Appl. Opt. **46**, 5933 (2007).

[37] J. R. Fienup, D. K. Griffith, L. Harrington, A. M. Kowalczyk, J. J. Miller, and J. A. Mooney, Proc. SPIE **4792**, 1 (2002).